Image processing pipeline for shear measurement

A. Guyonnet[1]

LPNHE, CNRS-IN2P3 and Universités Paris 6 & 7, 4 place Jussieu, F-75252 Paris Cedex 05, France

August 29, 2016

ABSTRACT

This report present the status, as of August 2016, of the shear measurement pipeline that has been developed at the LPNHE to measure the mass of clusters of galaxies observed by the SuprimeCam instrument at the Subaru Telescope. As of today, all the processing steps from the raw images to the shear profiles of the clusters have been implemented. The pipeline also successfully implements two new features that shall improve the precision of the shear measurement of the galaxies: the brighter-fatter correction of the images and a high precision global astrometry of the objects.

Contents

Introduction

This report presents the pipeline that is being developed at the LPNHE to process the images of the *Weighing the f_{gas} clusters* proposal (Astier, P. & al 2015), an extention of *Weighing the giants*, a project that has measured the weak-lensing masses of 51 galaxy clusters from their shear profile, found from the distortion of the shape of background galaxies (von der Linden et al. 2014).

A large sample of dynamically relaxed clusters allows to determine the gas-to-total mass ratio (f_{gas}) which provide an excellent estimate of the ratio of the cosmological parameters Ω_b/Ω_m (Mantz et al. 2014). The test is expected to remain competitive with (and complementary to) other cosmological probes over the next decade, the key requirement being additional weak lensing observations of clusters. The study of the systematics of *Weighing the giants* has shown that robust photometric redshift estimates of the lensed galaxies is critical, while only 6 clusters of the current sample have 5-band observation.

The *Weighing the f_{gas} clusters* observation provides additional observations of 12 f_{gas} clusters which will help delivering robust photo-z's. The French part of the consortium also aims at contributing a second pipeline to this project. In particular, our pipeline implement two improvements with respect to current shear measurement methods: an high precision astrometry code named GlobalAstrometry[1], and a brighter-fatter correction. The need for a precise astrometry is stringent because an error on the object's position translates into a bias on the determination of its shape. In the meantime, the removal of an instrumental signature such as the brighter-fatter effect is also required, because it biases the determination of the Point Spread Function (PSF), a critical ingredient of the shape measurement.

Weighing the giants has estimated that the total uncertainty is a combination of a ≈20% statistical precision of each cluster weak-lensing mass (Applegate et al. 2014), a ≈15% intrinsic scatter between weak lensing masses and true (3D overdensity) for the 12 relaxed clusters in the current sample, because of triaxiality and projection effects(Applegate et al. 2016), plus a systematic uncertainty of 4% due to the calibration of the masses of the 6 clusters without 5-filter imaging for photo-z's from clusters which have 5-filter photometry (and thus accurate photo-z's). Lastly, systematic uncertainties due to shear calibration, the assumed mass distribution, and the photo-z's are at the 4% level. Hence, for the current sample of 12 clusters, the total uncertainty on the average mass is $\sqrt{(20\%)^2/12 + (15\%)^2/12 + (4\%)^2 + (4\%)^2} \approx 10\%$. By completing weak lensing observations of 31 f_{gas} clusters, with 5-filter photo-z's for all clusters, the precision can be improved to $\sqrt{(20\%)^2/31 + (15\%)^2/31 + (4\%)^2} \approx 6\%$. Anticipating better control of the systematic uncertainties from on-going simulation efforts and improvements of reduction procedures (4% → 2%), a final precision of 5% is expected. This work adress this last aspect.

---

[1] http://supernovae.in2p3.fr/~astier/gastro/

Section 1 of this report describe the observations. It gives an overview of the optical characteristic of the Suprime-Cam imager at the Subaru Telescope and present the science and calibration dataset that is processed by the french pipeline.

Section 2 describes the pipeline, going from the raw images to the shear profile of the clusters. §2.1 present the overall pipeline design. A new feature of the image analysis, the correction of the brighter-fatter effect, is presented §2.2. This preprocessing step is followed by the flatifelding (§2.3) and a first detection of the astrophysical objects in the fields (§2.3.2). The method to classify them as stars or galaxies is described §2.3.3. For each object, a position (§2.4) and a flux is determined (§2.5). A precise astrometry for the background galaxies is particularly important in the context of shear measurement : the strategy here has been to use a simultaneous astrometry. The magnitude of the galaxies are needed to determine their redshift. The strategy is presented §2.6. Lastly the shear profile of the clusters needs a shape measurement for each galaxy (§2.7). The last section (3) discuss the question of the calibration of a shear estimator.

1. Instrument and Dataset

1.1. Instrument

The observations have been performed using the Suprime-Cam instrument, a CCD camera mounted on the Subaru Telescope, an 8.2m located at the Mauna Kea in Hawaii. The imager is made of ten CCDs, arranged in a 5x2 pattern (a total effective area 15cm x 12cm), providing a field of view of 34' x 27' with a pixel scale of 0.20"[2].

The camera was first installed in 2000 and is still in operation now, in 2016. In two occasion, 2001 and 2008, the CCDs of the focal plane have been replaced. From 2001 to july 2008 (MJD 54648), 10 thin CCDs MIT/LL, each read by 2 amplifiers, were in operation[3]. After 2008/07, the camera underwent a major upgrade and the focal plane was replace with 10 thick CCDs Hamamatsu (4 amplifiers), 2048×4096 pixels, back-illuminated, 15 μm on a side. This second camera is called Suprime-Cam2 throughout this report. Between July 29, 2008 and December 3, 2008 The camera response is known to have had problems with the linearity in the low counts. The issue was settled in December 2008 after a change in the threshold voltage for the readout system. Another change in the readout voltage of channel 9 took place in October 2010. In July 2nd, 2011, an hardware incident occured: An extensive amount of coolant (ethylene glycol) leaked out of the top unit of Suprime-Cam down to the primary mirror[4]. Open-use observations utilizing Suprime-Cam2 resumed on the night of July 15, 2012, after recovery work has included meticulous inspection and cleaning of the affected areas. Follow-up efforts during the summer of 2013, when the primary mirror was thoroughly cleaned, realuminized, and inspected, concluded that there are no visible effects either from the coolant or from the washing.

1.2. Dataset

1.2.1. Clusters sample

The dataset of clusters has been constituted by selecting those observed by Suprime-Cam with a known redshift (from the Planck catalog) around 0.5. The search of such objects was done

using the online archive SMOKA (http://smoka.nao.ac.jp/) and requesting observations with a RA/DEC position ± 10" of the clusters centroid provided by the Planck catalog. All the observations that match this criteria have been downloaded. They span 10 years of Suprime-Cam operation, between 2002 and 2012. The table 1 lists the clusters that constitutes the sample: the first column indicates the redshift, the second, the gas mass, while the 8 remaining columns indicates the number of images for a given band.

1.2.2. Calibration frames

The calibration frames refer to bias images (0 second exposure) and flatfield images (an image of a uniformly lit source). The bias images are combined by median-stacking in order to build a master-bias which is subtracted to all the images so as to remove electronic signatures. The flatfield images are combined to build master-flats that are used to correct for varying pixel sensitivity. There are two types of flatfield images: the twilight flats that are used to build the master-flats, and the domeflats that are needed to derive the correction for the brighter-fatter effect.

The process of collecting the calibration frames from the SMOKA archive is iterative: the amount of frame needed depends on the number of successive reconfiguration of the camera, as well as of the stability of the instrumental response in each interval. A first approach has been to request at least 10 bias and flatfield frames within ± 10 days around each exposure date. For this purpose, a script is used to automatically search the SMOKA archive. In total, 1635 calibration frames have been collected resulting in 31 intervals, but with some missing bands for a few dates. A study of the stability of the instrument has been done so has to gather the intervals within periods with proven stable patterns. As a result[5], it has been found that calibration frames are stable within periods that correspond to operation on the camera. Three main configurations of the camera are relevent for the science frames:

1. from 06-20-2001 to 06-30-2001, (MJD 52080-52090)
2. from 06-30-2001 to 07-01-2008, (MJD 52090-54648)
3. from 07-01-2008 to 04-06-2011, (MJD 54648-55657)

For the first period, the CCDs have an important non-linear response as well as several pixel cosmetic defects. The CCDs of the second period are better, but dynamic range is limited to 35 000 ADUs (von der Linden et al. 2014). The third period should be further splitted into two intervals because there were known linearity problem from july to december 2008. Later on, instability on CCD9 have been reported, until it was corrected in november 2010 (MJD 55501). Then, calibration frames can be collected until the incident (MJD 55744). The period between MJD-55501 and MJD-55744 shall be called 3b hereafter.

2. Image processing and production of catalogs of galaxies

2.1. Technical features of the shear pipeline

The purpose of the image reduction pipeline is to associate each cluster with a catalog of background galaxies with astrometry, photometry and shape measurement and the associated uncertainties. Trivially, the position of the galaxies are needed to build the shear profile of the cluster, but it is also an ingredient of the

---

Cluster	Redshift	Gas Mass	Filter							
			B_j (#)	V_j (#)	R_C (#)	I_C (#)	g_{SDSS} (#)	r_{SDSS} (#)	i_{SDSS} (#)	z_{SDSS} (#)
PLCK G44.7-51.3	0.5027	8.12	7	16	13	10	0	0	0	10
PLCK G45.3-38.5	0.5889	7.68	12	6	12	6	0	0	0	31
PLCK G73.3+67.5	0.6070	6.26	0	0	0	0	15	5	8	0
PLCK G111.6-45.7	0.5410	9.69	29	45	25	12	0	0	0	44
PLCK G144.9+25.1	0.5840	8.02	17	19	18	15	0	0	3	42
PLCK G155.3-68.4	0.5400	7.33	0	0	0	0	0	4	0	0
PLCK G180.3+21.0	0.5460	14.0	30	17	30	18	0	0	3	41
PLCK G201.5-27.3	0.5392	8.18	11	12	28	18	0	0	20	30
PLCK G211.2+38.6	0.6730	7.22	12	6	9	6	0	0	3	12
PLCK G228.2+75.2	0.5444	9.49	10	7	18	5	0	0	3	21

Table 1. List of the clusters dataset. The Gas Mass is the gas mass within R500, the radius corresponding to a density contrast of 500. Details about the filters are available online : http://www.naoj.org/Observing/Instruments/SCam/sensitivity.html.

shape estimator. The estimation of the photometric redshift of the objects necessitates high precision photometry in 5 bands. Shape measurement is currently the most challenging step in weak lensing experiments, several teams throughout the world are assessing various approaches. Here, we develop a moment based, maximum likelihood method, following Bernstein et al. 2016.

To keep track of the status of the processing at each step, the pipeline is run using Pipelet[6], a free framework allowing for the creation, execution and browsing of scientific data processing pipelines. It allows to process the images in a sequence of steps where the input of each process is the output of the previous one. It also keeps track of the version at each stage. It allows to dispatch the computational tasks on parallel architecture, which is useful for a large data set with high computation cost.

The sequence to progress from the raw images to the shear measurements are schematically represented on the flowchart figure 1. At the exception of the non-linearity correction and the cross-talk correction, they have all been implemented and run. The algorithms used are the one that were developed for the SNLS pipeline, except for the brighter-fatter correction that is a new feature of weak lensing analysis. The SNLS algorithms present the advantages that they have been largely debugged and that they are versatile so that they can be used on any multichip mosaic camera.

2.2. Brighter-fatter correction

The brighter-fatter effect refers to the dependence of the apparent size of the stars, as measured by optical CCD telescopes, with respect to their luminosity (Guyonnet et al. 2015, G2015 hereafter). It can be observed by looking at the moments of the stars as a function of the flux. The effect is a manifestation of the repulsion of the charges already collected within the pixels on the incoming ones. It results in an increase of the instrumental PSF that is proportional to the brighness of the objects (G2015). It affects all the sciences analysis that rely on an accurate PSF model of their CCD instrument, with first and foremost weak lensing. Many teams are currently implementing and testing the performance of methods that correct for it at the pixel level, before the step of modeling the PSF (G2015). Two approches are being explored to determine the undistorded distribution of the charges: either from electrostatic simulations, or, by using the effect as it manifests in flatfield frames, to determine a model of the defor-
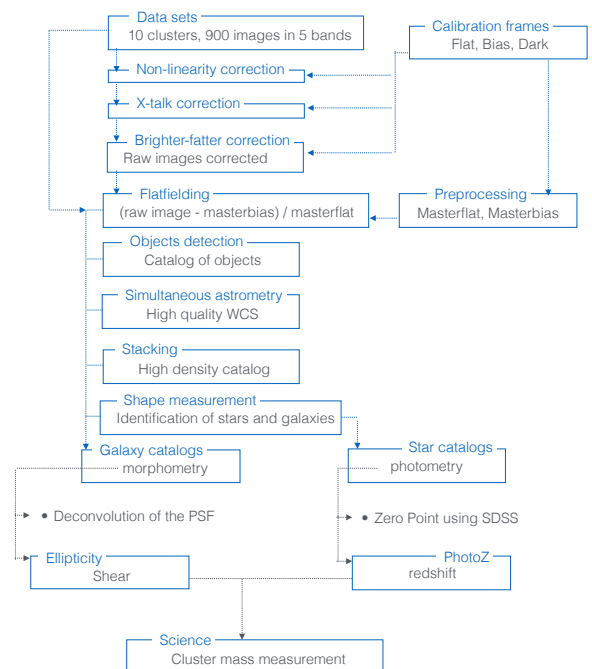
---

[6] http://supernovae.in2p3.fr/~betoule/pipelet/

Fig. 1. A flowchart showing the main stages in the production of the shear catalogs.

mation of the pixels. The fisrt strategy is difficult and still under development. It requires a detail knowledge of the devices that is usually not available. The second method has been the only one implemented and tested in shear pipelines: HSC and DES have concluded that the correction restores a control on the PSF that is acceptable given there requirements.

The second approach has also been implemented in this pipeline, divided into four steps:
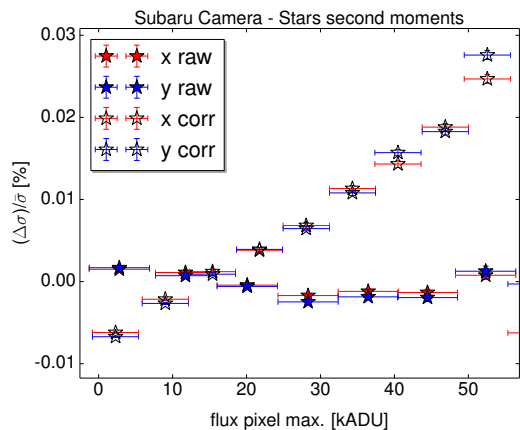
Fig. 2. The brighter-fatter effect on Suprime-Cam2 (period 3b) is shown by the empty stars, and after correction, by the filled stars.

1. Build the image difference of a pair of domeflats with same illumination conditions, which removes spatial variation of the illumination pattern.
2. Measure the spatial correlations between pixels.
3. Determine a model of the boundaries displacement (express in fraction of pixel per ADU) that is tuned on the correlations measurement, plus an assumption on the profile of the decrement.
4. Apply the model to the raw science images.

For the first step, domeflat pair illuminations that are stable at a level better than 3‰ are selected. This cut has a good outliers rejection efficiency, although a better selection criteria should be determined: 1 or 2 outliers remains and contribute to slighlty overestimate spatial correlations. It is also important to mask bad pixels. Typically, it removes ∼ 30K pixels per amplifier from the measurement. Glowing edges are also masks, which removes an additonnal ∼ 80K pixel for amplifiers at the edges of the CCDs. For the second step, it is important to measure spatial correlation as far as possible. This requirement directly relates to the available statistics: with about 200 points (for instance for period 3b), the correlations are detected up to a distance of 4 pixels. For the third step, to convert correlation into estimation of boundary shifts, an assumption on the smooth decay of the effect is added. It was found to have a negligeable impact on the overall uncertainty of the correction (G2015). For the last step, an assumption needs to be made on the initial profile of the charges to be redistributed, it introduces the biggest contribution to the uncertainty budget of the correction (G2015).

The correction coefficient must be determined for each configuration of the camera and each amplifier. The performance of the correction is assessed by comparing the second moments of the stars with and without applying the correction. The result is shown figure 2.

2.3. Calibrated images and objects detection

2.3.1. Master-bias subtraction and flatfielding

A calibrated image, or "flatfielded" image is a raw image minus a master-bias, divided by a master-flat minus a master bias. Master-bias and master-flat are created for each period. Master-bias are subtracted to science images and flatfields after adjusting the medians of the overscans to adjust the level of the images.
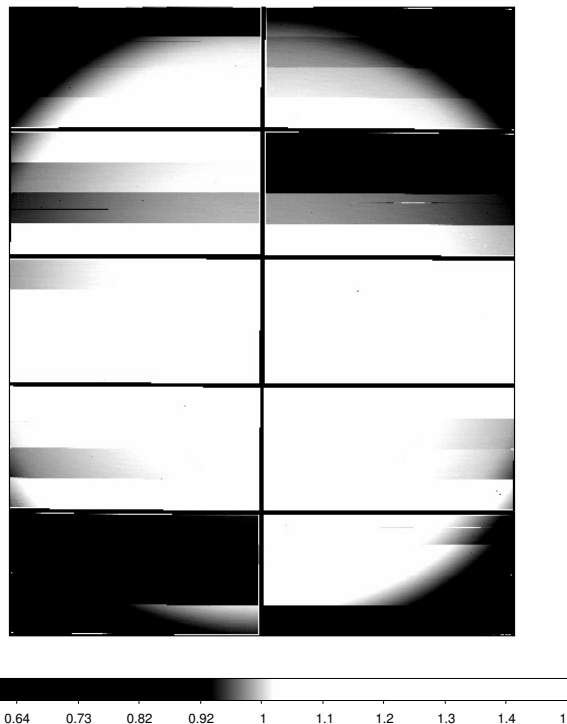
Fig. 3. i_{SDSS}-band master-flat for the period 3.

For the period 2, the master-bias shows a readout noise of ≈ 2 ADU, or 6 e⁻. The flatfields have a rms 2-6 permil for all the CCDs expect the 0 which has a 1.7% rms. Suprime-Cam data frames have a shadowed area on the top of the FOV (see figure 3), which is due to vignetting by the auto-guider (AG) probe. This shadowed area can not be flatfielded correctly, and the flux calibration is difficult to perform (von der Linden et al. 2014).

The output of the production is one repository per cluster, with one repository per exposure and per CCD. In each one, there is the calibrated image, a link to the raw image, the master-bias and the master-flat, plus a weight map of the pixels. A preview that combines all the calibrated segment of an exposure of PLCK G180.3+21.0 in R_C-band is shown as an illustration on figure 4. An unstability of two amplifiers of the CCD9 is visible on the lower left part of the field.

2.3.2. Masks and objects detection

The objects in the frames are detected using Sextractor (Bertin, E. & Arnouts, S. 1996). For each segment, a background is estimated as well as a saturation level so that saturated pixel are flagged. Bad pixels, cosmic rays, satellite trails are also detected and set to zero in the weight maps. An object catalog is then produced, and point-like objects are used to derive an image quality (IQ) estimate. The sky background map is then subtracted from the image. Additionally, computation of adaptive Gaussian-weighted second moments is performed on the objects of the catalog, as well as aperture photometry for the purpose of photometric calibration. The base flux of the star catalog is a corrected isophotal flux if not crowded, the flux within a Kron-like elliptical aperture otherwise.[7]

---

[7] *FLUX-BEST* from SExtractor, i.e. *FLUX-ISOCOR* if not crowded, *FLUX-AUTO* otherwise.

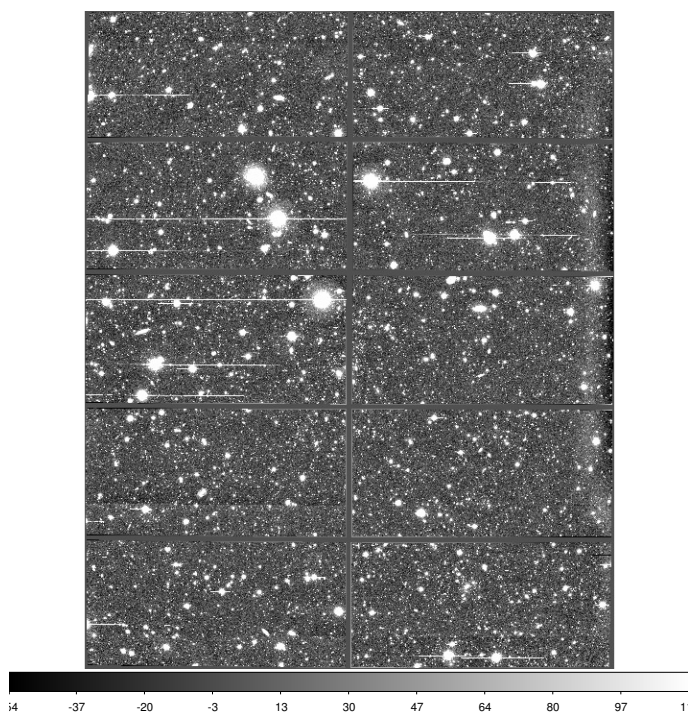**Fig. 6.** Illustration of the IQ spatial variation over the focal plan (R_C band).

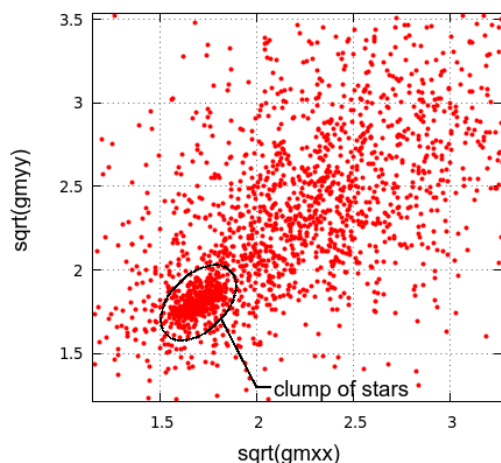**Fig. 4.** Preview of PLCK G180.3+21.0 cluster in R_C-band.

Fig. 5. Detected objects on a given CCD dispersed as a function of moments: the clump of objects in the lower left corner corresponds to the stars.

2.3.3. Star/galaxy classification

The discimination between stars and galaxies is based on the method proposed by Astier et al. (2013) that is further refined to take the spatial variation of the IQ into account. The method to select the stars is to bin the objects detected into a 2-D histogram of the second moments. The clump of the stars is modeled as a 2-D Gaussian distribution and a first sample of stars is selected within a 5σ ellipse around the clump in the (gm_{xx}, gm_{yy}) plane (figure 5). Then, these objects are used to fit a smooth model of the IQ variation within the frame (a 4th order polynomial is used), and the first step is done once again, after having corrected each object by the local IQ. The second pass is necessary, especially for the CCDs in the corner of the focal plane (figure 6). The catalog of galaxies is the compementary of the object selected as stars at the second pass.
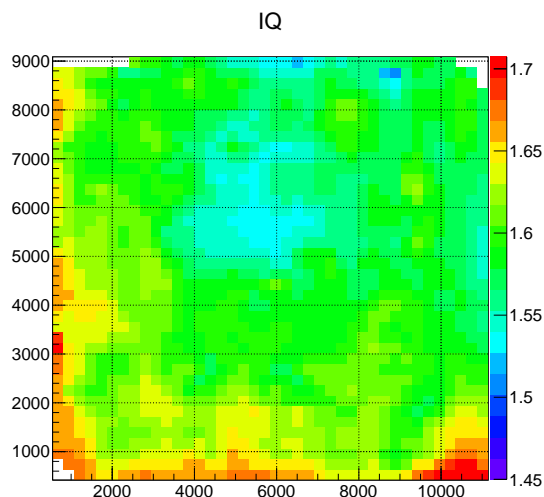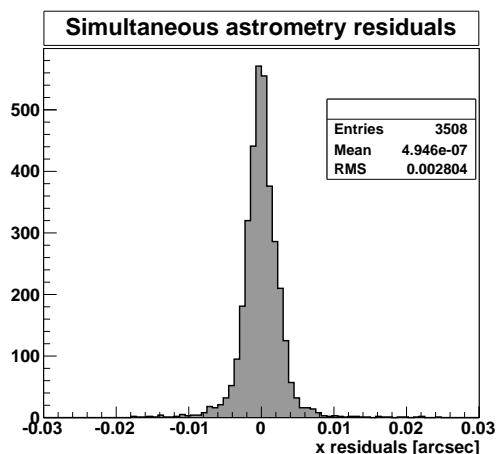
Fig. 7. RMS residuals of simultaneous astrometry is below 3 miliarcsec (objects magnitude below 19).

2.4. Simultaneous astrometry

The astrometry is obtained in two steps:

1. First, a match with the USNO catalog is performed to improve the WCS. A model of the focal plan geometry is determined by using several exposures with the same pointing and orientation, selecting the stars and matching it to a reference catalog. the outcome is more accurate WCSs (>0.3 arcsec).
2. The second step consists in adjusting simultaneously the WCS and the positions of the objects. The WCS are adjusted for the series of image of a given field (at least 10 to reflect measurement noise). Then, their catalogs of objects are associated to an external catalog to fix the sideral coordinates. Lastly, the sideral positions of common objects and the WCS are adjusted, taking the measurement errors into account.

The residuals of the simultaneous astrometry are very good : 2.8 mas for R_C (figure 7), 2.1 mas for V_j, 2.4 mas for i_{SDSS}, 4.8 mas for V_j, 4.5 mas for z_{SDSS} for bright objects. The level of the residuals depends on shot noise (brightness dependent), on the atmosphere and on the sensors. The CCDs were HyperSuprime-Cam prototype and in the publication von der Linden et al.

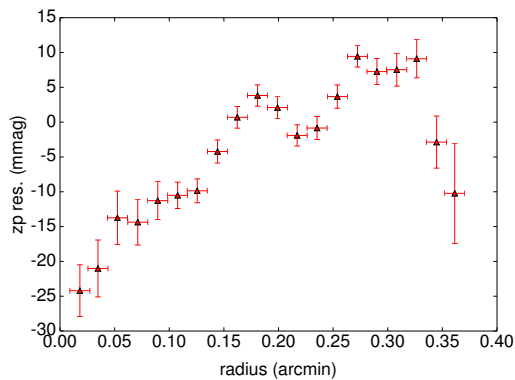**Fig. 8.** Illustration of the IQ spatial variation over the focal plan (R_C band).

Fig. 9. The effective passband of Suprime-Cam at the Subaru Telescope : transmission of the optics, reflectivity of the mirror, filters transmission and QE of CCD's.

(2014) it is reported that the division between pixels may not be straight lines but could be curved. I should look at the spatial distribution of the residuals to see if I can confirm that. But the level of the residuals are already about five time better than current weak lensing surveys (Jarvis et al. 2016). The performance of the astrometry is particularly important for shape measurment because an error δx_0 inflates the moments $gm_{xx} \propto \delta x_0^2$.

2.5. Photometry

The photometric calibration is anchored to the SDSS AB magnitude system[8]. The zero point are found by matching a selection of high signal-to-noise stars with calibrated stars found on the SDSS footprint. To do so, the star positions are transformed in sideral coordinates and matched to the stars in the SDSS catalog if they lie within a 0.4 arc second distance and if smag > 0.1. A color transformation between SDSS and Subaru is fitted and a zero point is extracted for each exposure and each CCD. There are a few exposures for which a CCD images a portion of the sky that does not fell on a SDSS strip, in which case, the average zero point of the surronding CCDs is used. There are also two cluster fields, PLCK G44.7-51.3 and PLCK G144.9+25.1, that do not fell on the SDSS footprint. The rms ~0.01% magnitude on the color transformation are spatially correlated. The figure 8 shows the radial variation of the zero points residuals. It is likely that the current flatfielding strategy is insufficient and that superflats (night time observations of 'empty' fields) should be used to mitigate residual variations (Regnault et al. 2009). This will be implemented in the future.

The zero points are used to assign magnitude to the galaxies. The stategy is to perform the photometry on a weighted stack of the exposures in all the band available for a given cluster. The alignment of the images that is needed prior to stacking benefits from the high quality WCS produced by the simultaneous astrometry. Technically, the photometry will be performed using sextractor in dual mode.

2.6. Photometric redshifts

The determination fo the shear profile of the clusters is best obtained using a photo-z-based method, which has smaller systematic uncertainty, than using the simpler color-cut method. However, it imposes additional cuts on the galaxy catalog, reducing the effective number of galaxies.
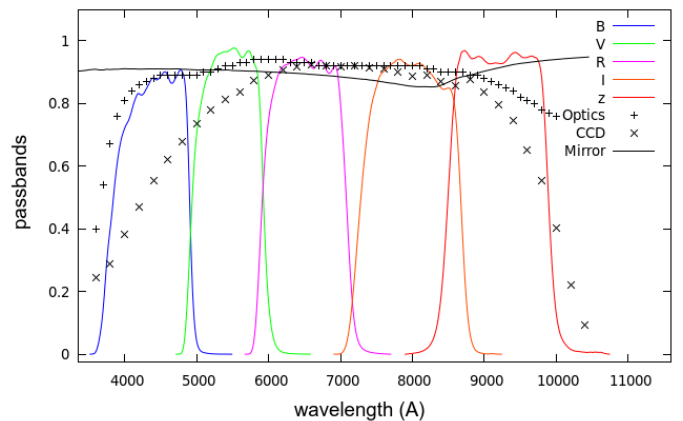
---

[8] http://skyserver.sdss.org/dr8/en/tools/search/sql.asp

The photometric redshifts are determined using the software developed by the SNLS collaboration (see §4.2 Kronborg, T. et al. (2010)). Galaxy spectral templates are defined using an evolution model (PEGASE.2) with a variety of galaxy SFR law and galaxy ages. A training set comprises a sample of galaxies with known spectroscopic redshift from the DEEP2 survey. The effective passband of Suprime-Cam at the Subaru Telescope has been found on the Subaru website and is shown figure 9.

2.7. Shape measurement of the background galaxies and shear profile of the clusters

2.7.1. Implementation of the Gauss-Laguerre method

The shear estimate is based on the Gauss-Laguerre method proposed by Bernstein & Jarvis (2002) [hereafter B&J method]. It defines galaxy ellipticity via the transformation that restores a "round" galaxy. The strategy is to find the shear η that when applied to the system make the image appear circular, and declare the galaxy shape to be this shear. The virtue of this definition is that the effect of a lensing distortion upon the galaxy shape is completely define by the multiplication of shear matrices.

The Gauss-Laguerre decomposition implements eigenfunctions of the 2-D quantum harmonic oscillator express as complex functions of 2 integers p,q. An image is decomposed as:

$$I(r, \theta) = \sum_{p,q \geq 0} b_{pq} \Psi_{pq}^{\sigma}(r, \theta)$$

Where b_{pq} are Gaussian-weighted moments of the intensity image:

$$b_{pq} = \sigma^2 \sum d^2 x I(\mathbf{x}) \bar{\Psi}_{pq}^{\sigma}(\mathbf{x})$$

And with:

$$\Psi_{pq}^{\sigma}(r, \theta) \equiv \frac{-(1)^q}{\frac{\pi}{\sigma}^2} \sqrt{\frac{q!}{p!}} \left(\frac{r}{\sigma}\right)^m e^{im\theta} e^{-r^2/2\sigma^2} L_q^{(m)}(r^2/\sigma^2)$$

The method to determine the b_{pq} is to assume a σ using a size matching condition $b_{11} = 0$, then find the least χ^2:

$$\chi^2 = \sum_i \frac{\left[I_i - \sum_{pq} b_{pq^0} \Psi_{pq}^{\sigma}(\mathbf{x_i})\right]^2}{var(I_i)}$$

observed galaxy image and reconstructed *intrinsic* shear
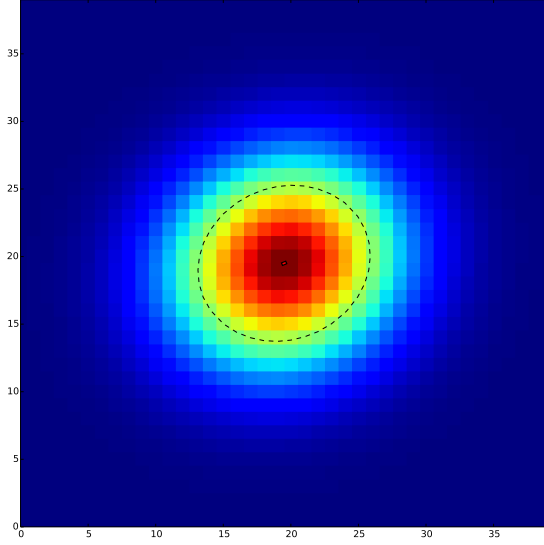

Fig. 10. Simulated elliptical galaxy and reconstructed intrinsic ellipticity after deconvolution of a gaussian PSF.

The circularity condition translates into $b_{20} = 0$ and the deconvolution of the PSF b_* is performed by inverting $\mathbf{C}(b_*)$ in the relation:

$$b^{obs} = \mathbf{C}(b_*) \times b^{int}$$

To get the instrinsic shape of the object b^{int}, which relates to shear η through the relation:

$$\eta = \frac{-2\sqrt{2}b_{02}^{int}}{b_{00}^{int} - b_{22}^{int}}$$

And from which ellipticities are defined as:

$$\epsilon_1^{int} = Re[tanh(\eta)]$$

$$\epsilon_2^{int} = Im[tanh(\eta)]$$

The deconvolution has been tested by simulated a galaxy with ellipticities $(\epsilon_1^{gal}, \epsilon_2^{gal}) = (0.100585, 0.099256)$, convolved by a Gaussian PSF. After deconvolution, the reconstructed galaxy ellipticities are found to be $\epsilon_1^{int} = 0.100571$ $\epsilon_2^{int} = 0.099285$ (figure 10). The high fidelity of the reconstructed galaxy validates the implementation of the B&J method.

2.7.2. Cluster shear profile

The measurements of the galaxies shape are performed in the R-band. The stacking of 10 exposures, of 240 seconds each, of the cluster field PLCK G180.3+21.0 (using SWARP - median method) increases the density of galaxies from 19 galaxies/arcmin^2 in a single image to 34 galaxies/arcmin^2 in the stacked images. The higher the signal-to-noise cut on the galaxies in the lensing analysis, the lower the shear measurement bias correction. In this pipeline the galaxies are selected with S/N>10. On a typical cluster field, it lefts 9 galaxies/arcmin^2.

Figure 11 shows the shear profile of cluster PLCK G180.3+21.0, using 7 exposures and selecting the galaxies with
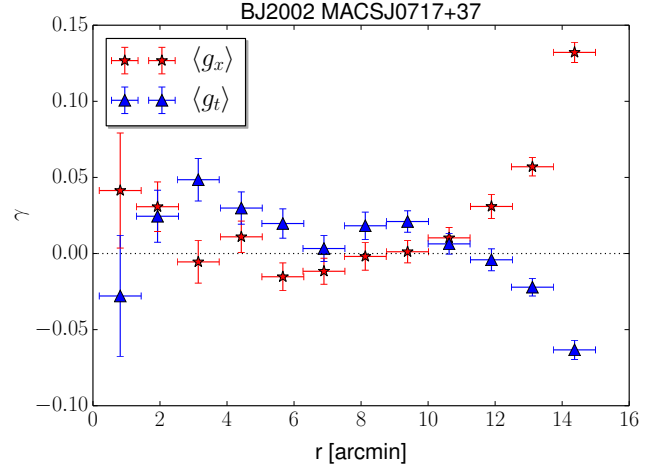

Fig. 11. The shear profile of the cluster PLCK G180.3+21.0, after deconvolution using the B&J method (R_C band).
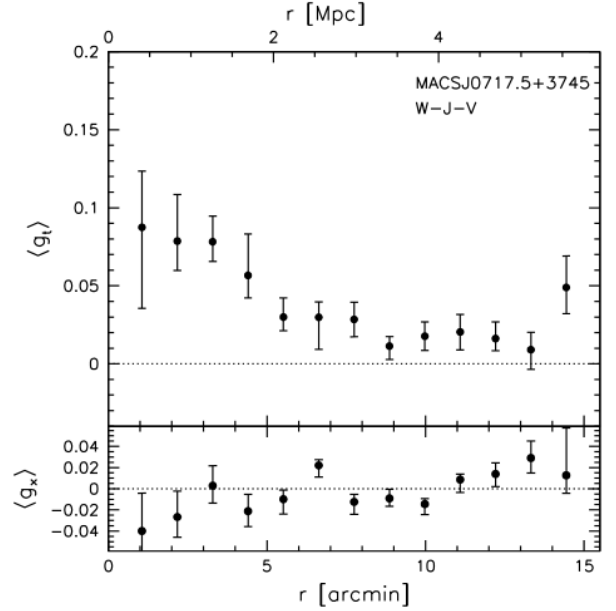

Fig. 12. Shear profile of PLCK G180.3+21.0 as measured by *Weighing the giants* (von der Linden et al. 2014).

magnitudes between 20 and 24. The values of the b^* coefficients are interpolated at the locus of each galaxy using a 3rd order polynomial. The tangential (γ_t) and cross (γ_x) decomposition of the shear corresponds to:

$$\gamma_t = -(\epsilon_1^{gal}cos(2\theta_C) + \epsilon_2^{gal}sin(2\theta_C))$$
$$\gamma_x = -\epsilon_1^{gal}sin(2\theta_C) + \epsilon_2^{gal}cos(2\theta_C)$$

With θ_C the angular position of the galaxy with respect to the center of the cluster.

The profile of the tangential shear γ_t of the distant galaxies obtained with the B&J method does not exhibit the expected signal near the center of the field (figure 12). It also presents a strong departure from zero of both components at the edges. It is known that the B&J method does not perform well with anisotropic PSF, which gets quite large towards the edge of the field of view (figure 13). From simulation, the estimated syhtematic error of the method is [1-4%] at a S/N [50-20] (Nakajima & Bernstein 2007). To correct for this bias, the re-gaussianization
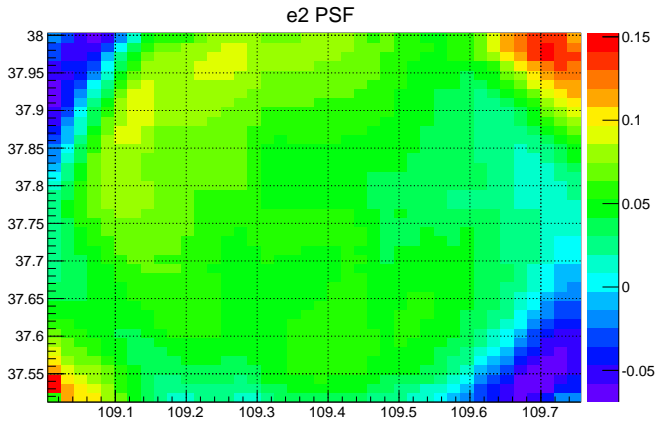
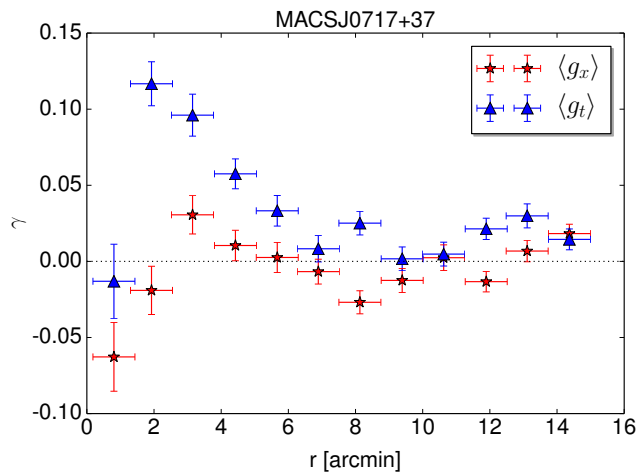**Fig. 13.** Spatial variation of the Psf ellipticity for the same field.

Fig. 14. The shear profile of the cluster PLCK G180.3+21.0, after deconvolution using a direct subtraction of the PSF moments at the locus of each galaxies.

method from Hirata & Seljak (2003) should be added to the deconvolution.

This result can be compared with the straightforward estimation of the galaxies' ellipticities from a direct subtraction of the PSF adaptative Gaussian weighted second moments (interpolated at the locus of each galaxy):

$$\epsilon_1^{gal} = \frac{(gm_{xx}^{gal} - gm_{xx}^{psf}) - (gm_{yy} - gm_{yy}^{psf})}{(gm_{xx}^{gal} - gm_{xx}^{psf}) + (gm_{yy}^{gal} - gm_{yy}^{psf})}$$

$$\epsilon_2^{gal} = \frac{2(gm_{xy}^{gal} - gm_{xy}^{psf})}{(gm_{xx}^{gal} - gm_{xx}^{psf}) + (gm_{yy}^{gal} - gm_{yy}^{psf})}$$

The centroid of the galaxies (first moments) where obtained from the positions derived from the stacked images. The figure 14 shows the result. The ellipticity of the edge of the field has disappeared, while a lensing signal (γ_t) is found with an amplitude compatible with the measurement from *Weighing the giants* (von der Linden et al. 2014).

3. Discussion

The fundamental problem of shear estimator techniques is that there are no standard sheared objects in the sky. The only strategy is to calibrate the relation between shape and shear against simulations of artificial galaxy images. For moment based techniques, as described in 2.7, the task is to assign some shape ϵ^{gal} to observed galaxy, then to derive from it an estimate of the applied lensing shear γ. The shape is quantified using the moments of the surface brightness distribution of a galaxy.

Schematically, it goes from:

Object $\rightarrow$ Moments $\rightarrow$ ϵ^{gal} $\rightarrow$ γ $\rightleftharpoons$ simulation.

The definition of ϵ^{gal} depends on the moment weighting strategy and, since there are no "standard shear" lenses on the sky, the shear estimator γ is calibrated against a simulation. There are currently several original attempts to go from the object(s) to the shear γ, but in any case, the question remains: does the method really measure gravitational shear ?

The different shear estimators can be separated into two groups: maximum likelihood methods and Bayesian methods. In both categories, there are various approaches that can be further distinguished as model fitting methods or moment-based, such as in this report.

For most methods, when looking at realistic scenarios (very faint objects with complicated shapes)[9], the measurements are found to be biased above the requirements of Stage IV Programs. This is why there are currently a strong activity of comparing methods (for instance the GREAT challenge Mandelbaum et al. (2014)).

Among the most promising method, The Bayesian Fourier Domain approach skips the estimation of galaxy shape properties (Bernstein et al. 2016). It relies on a high signal-to-noise observation of a subset of the survey region to provide an analytic expression for the probability P(M|γ).

Acknowledgements

References

Applegate, D. E., von der Linden, A., Kelly, P. L., et al. 2014, MNRAS, 439, 48 1
Applegate, D. E. et al. 2016, Mon. Not. Roy. Astron. Soc., 457, 1522 1
Astier, P., El Hage, P., Guy, J., et al. 2013, A&A, 557, A55 5
Astier, P. & al. 2015, CFHT proposal for 2015A 1
Bernstein, G. M., Armstrong, R., Krawiec, C., & March, M. C. 2016, MNRAS, 459, 4467 3, 8
Bernstein, G. M. & Jarvis, M. 2002, AJ, 123, 583 6
Bertin, E. & Arnouts, S. 1996, Astron. Astrophys. Suppl. Ser., 117, 393 4
Guyonnet, A., Astier, P., Antilogus, P., Regnault, N., & Doherty, P. 2015, A&A, 575, A41 3
Hirata, C. M. & Seljak, U. 2003, Phys. Rev. D, 68, 083002 8
Jarvis, M. et al. 2016, Mon. Not. Roy. Astron. Soc., 460, 2245 6
Kronborg, T., Hardin, D., Guy, J., et al. 2010, A&A, 514, A44 6
Mandelbaum, R. et al. 2014, Astrophys. J. Suppl., 212, 5 8
Mantz, A. B., Allen, S. W., Morris, R. G., et al. 2014, MNRAS, 440, 2077 1
Nakajima, R. & Bernstein, G. 2007, AJ, 133, 1763 7
Regnault, N., Conley, A., Guy, J., et al. 2009, A&A, 506, 999 6
von der Linden, A., Allen, M. T., Applegate, D. E., et al. 2014, MNRAS, 439, 2 1, 2, 4, 5, 7, 8

---

[9] It should also be noted that when we write $\epsilon^{obs} = \epsilon^{gal} + \gamma$, it holds only for $\epsilon^{gal}, \gamma \rightarrow 0$. There are several case were we should go to higher terms.

Appendix A: Linearity of Suprime-Cam1

The linearity of Suprime-Cam has been studied twice in august 28 and 30, 2002. The measurement consists in taking domefltats with increasing exposure times and looking at the residual of a linear fit of the flux as a funciton of exposure time. The results varies between a few permil to up to 1% at 30kADU. It is unclear if the condition were stable during the measurement. See http://smoka.nao.ac.jp/help/help_supdetail.jsp.